Acta Biomaterialia 101 (2020) 403–413

Contents lists available at ScienceDirect

Acta Biomaterialia

journal homepage: www.elsevier.com/locate/actbio

Full length article

The regional-dependent biaxial behavior of young and aged mouse skin: A detailed histomechanical characterization, residual strain analysis, and constitutive model

William D. Meador[a], Gabriella P. Sugerman[a], Hannah M. Story[b], Ashley W. Seifert[c], Matthew R. Bersi[d], Adrian B. Tepole[e], Manuel K. Rausch[a,f,g,*]

[a] Department of Biomedical Engineering, University of Texas at Austin, Austin, TX, USA
[b] Department of Biological Sciences, University of Texas at Austin, Austin, TX, USA
[c] Department of Biology, University of Kentucky, Lexington, KY, USA
[d] Department of Biomedical Engineering, Vanderbilt University, Nashville, TN, USA
[e] Department of Mechanical Engineering, Purdue University, West Lafayette, IN, USA
[f] Department of Aerospace Engineering and Engineering Mechanics, University of Texas at Austin, Austin, TX, USA
[g] Oden Institute for Computational Engineering and Sciences, University of Texas at Austin, Austin, TX, USA

ARTICLE INFO

Article history:
Received 8 June 2019
Revised 8 October 2019
Accepted 10 October 2019
Available online 12 October 2019

Keywords:
Murine
2-photon microscopy
Histology
Prestrain
Hyperelastic
Stress
Stiffness, aging

ABSTRACT

Skin fulfills several vital functions, many of which are dependent on its mechanical properties. Therefore, as mice have become an invaluable model for skin research, determining murine skin's mechanical properties is important. Specifically, skin's mechanical properties are important for functional tests as well as for prognostic and diagnostic purposes. Additionally, computational simulations of skin behavior are becoming commonplace, rendering accurate models of murine skin's constitutive behavior necessary. To date, our knowledge of mouse skin mechanics shows significant gaps. For example, there are no comprehensive reports correlating skin's mechanical properties with region, age, and direction. Moreover, mouse skin's residual strain behavior has not been reported on. In our current work, we set out to fill these gaps. Based on histology, 2-photon microscopy, and planar biaxial testing, while accurately tracking various reference configurations, we report on differences in gross structure, microstructural organization, and constitutive response of skin, and cast those properties into a versatile Fung-type hyperelastic constitutive law for three reference configurations. Our data is the most comprehensive report contrasting the mechanical properties of young (12 weeks) and aged (52 weeks) mouse skin and will, thus, be valuable to basic science as control data, and provide accurate constitutive laws for mouse skin modeling.

Statement of significance

Our findings are significant as they fill several gaps in our understanding of mouse skin mechanics. This is particularly important as mouse skin is becoming a frequent and critical model of human skin for cosmetic and medical science. Specifically, we quantified how mechanical properties of mice skin vary with age, with location, and with direction. Additionally, we cast our findings into constitutive models that can be used by others for predictive computer simulations of skin behavior.

© 2019 Acta Materialia Inc. Published by Elsevier Ltd. All rights reserved.

1. Introduction

Skin plays a vital role in providing a physical barrier against environmental insults to our body, and its mechanical properties are critical for supporting this function [1]. As a classic collagenous soft tissue, skin exhibits a nonlinear stress-stretch response that follows from the inherent properties of its extracellular matrix constituents - ostensibly collagen and elastin - as well as their microstructural organization and interplay [2]. Although, usually perceived and modeled as a hyperelastic material, skin also exhibits viscoelastic traits such as hysteresis, stress-relaxation, creep, and permanent set. These properties arise from the inherent solid

---

[*] Corresponding author at: University of Texas at Austin, 2501 Speedway, EER Building, Room 7.620, Austin, TX, USA.
E-mail address: manuel.rausch@utexas.edu (M.K. Rausch).

https://doi.org/10.1016/j.actbio.2019.10.020
1742-7061/© 2019 Acta Materialia Inc. Published by Elsevier Ltd. All rights reserved.

phase viscoelasticity of its extracellular matrix proteins and their interactions with the interspersing interstitial fluid [3–5]. Moreover, the relative distribution and density of these constituents render skin a multi-layered structure whose constitutive behavior depends on direction and region, and varies with depth, i.e., skin behavior is anisotropic and heterogeneous [6–8].

Dermal properties are not temporally invariant, but rather evolve throughout our life time [1,9]. Even as adults, skin alters its constitutive behavior in response to continuous environmental exposure [10], hormonal changes [11], disease [12], bacterial invasion, and scarring [13]. Thus, characterization of skin's constitutive behavior is not only of basic scientific interest but is also of diagnostic importance and of prognostic relevance.

For skin research, mice have emerged as a powerful biological model system. Their relatively low cost, easy husbandry, fast life-cycle, and their genetic malleability have led to the development of mouse models for many skin disorders [14–16]. Because of skin's mechanical behavior being of importance to both basic science, cosmetic science, and medical science there has very recently been an accelerated push to characterize mouse skin constitutive behavior [8,9,17–22]. However, to date there are several key pieces missing from our understanding of mouse skin mechanics.

First, mouse skin has never been tested under biaxial loading. Previous studies have uniaxially tested mouse skin in two or more directions, thus, quantifying its anisotropy [8,22]. However, those tests don't elicit the bi-directional coupling mode between dermal constituents and are thus insufficient to inform constitutive models of the planar biaxial behavior of skin [23,24]. Consequently, there are currently no sufficiently informed constitutive models of mouse skin. Also, mouse skin has exclusively been tested relative to a stress-free *in vitro* reference configuration. In other words, none of the available data have quantified the amount of *in situ* residual strain. Filling this particular gap is vital, because *in situ* residual strain results from deposition of matrix proteins by resident synthetic cells at a given prestretch. Thus, residual strain is maintained via continued physiological matrix turn-over and may therefore be a critical marker of tissue health [25–27]. Moreover, models of mouse skin based on a stress-free *in vitro* reference configuration are not predictive of the *in situ* behavior. We and others have shown that neglecting residual strain in models of other soft collagenous tissues can significantly alter interpretations of experimental data [28,29]. Additionally, there are currently no explicit reports on how mechanical properties of mouse skin vary with region.

To fill these gaps in our knowledge, the objective for the current work is to provide a comprehensive analysis of the biaxial constitutive behavior of murine skin - including regional-and age-dependence (12 weeks, i.e., young, *versus* 52 weeks, i.e., aged), microstructural composition, and residual strain - and use these data to inform an appropriate constitutive model.

2. Materials and methods

All animal procedures described here were approved by the Institutional Animal Care and Use Committee at the University of Texas at Austin under #AUP-2017-00078. Furthermore, we strictly adhered to NIH's Guide for Care and Use of Laboratory Animals.

2.1. Sample preparation

Following the humane sacrifice of 12 week (young) and 52 week (aged) male C57BL/6 mice via CO_2 inhalation, we removed the hair from dorsal and ventral skin regions using clippers and a chemical depilatory agent (Nair, Church & Dwight Co., Inc., Ewing, NJ, USA). Next, we applied an ink stamp of known dimensions (8 mm × 8 mm square) to dorsal and ventral skin regions at multiple sampled locations in this *unloaded in situ configuration*. From these regions, we excised up to four stamped, dorsal and two stamped, ventral skin samples.

2.2. Histology

Upon excision, we immediately fixed 12 skin samples (3 per young/aged, dorsal/ventral group from a total of 3 animals) in 10% neutral buffered formalin for 24 h, then transferred them directly to 70% ethanol. A commercial histology service (Histoserv Inc., Germantown, MD, USA) prepared all histological slides by embedding them in paraffin, sectioning them transversely to a thickness of 5 µm and staining them with Masson's Trichrome. In house, we additionally stained sections with Picrosirius Red. We subsequently acquired histological images on an upright microscope (BX53 Upright Microscope, Olympus, Tokyo, Japan), where we sampled several representative regions of each section at 10x magnification. To quantify relative mass densities of structural constituents from Masson's Trichrome stains (collagen, cytoplasm/muscle) via area fractions, we utilized a custom MATLAB program [30]. To measure layer thicknesses, we utilized a custom MATLAB program which interactively selects orthogonal distances in Masson Trichrome images based on expected constituents within layers (i.e., epidermis – cellular layer, dermis – collagen, subcutaneous fat – clear fatty region, and muscle – organized muscular tissue). For each image, we sampled the thicknesses of the layers at three locations and averaged the values, avoiding areas of hair follicles.

2.3. 2-Photon microscopy

Post-mortem and upon excision, we transferred 12 skin samples (3 per young/aged, dorsal/ventral group from a total of 3 animals) to a 2-photon microscope (Ultima IV, Bruker, Billerica, MA, USA) for the *in vitro* collagen fiber orientation analysis via Second Harmonic Generation (SHG). We acquired all images epidermis up using a 20x water immersion objective (XLUMPLFLN, Olympus, Center Valley, PA, USA) at an excitation wavelength of 900 nm. We epi-collected the backscattered SHG through a PMT channel filter (460 ± 25 nm) and acquired a z-stack of images with a step size of 10 µm until the SHG intensity diminished (∼150 µm) at several different locations in the center of the tissue. Additionally, for the *in situ* analysis, we imaged depilated skin regions without excisions, but post-mortem, of 3 young and 3 aged mice using the same 2-photon microscope, objective, and imaging parameters, by placing the recently sacrificed animal directly under the 2-photon objective. In those animals, we imaged dorsal and ventral skin regions, amounting to the same group sizes as for the *in vitro* imaging, see above.

To analyze the SHG images, we used ImageJ-FIJI OrientationJ (National Institutes of Health, Bethesda, MD, USA) using its orientation distribution analysis with a Gaussian gradient method [31,32]. We verified this method against synthetic images of fibers that were sampled from a known distribution function. Subsequently, we fit a symmetric von Mises distribution to the raw data to estimate the distribution's location parameter $\tilde{\mu}$ and localization parameter $\tilde{\kappa}$ as a function of imaging depth [33]. Supplementary Fig. S1 depicts above pipeline and demonstrates the invariance of our approach to image angle.

2.4. *In situ* residual strain calculation

Upon excision, we floated 52 skin samples (13 per young/aged, dorsal/ventral from a total of 13 animals) on a layer of 1x PBS with the epidermal side up. In this approximately stress-free configuration, *unloaded in vitro configuration*, we photographed the specimens with their stamped profile clearly visible on a calibrated grid and within minutes of excision. Until biaxial testing, see Section 2.5, we stored those samples at 4 °C in 1x PBS. To compute *in situ* residual strain, we identified the coordinates of the stamp's corners from above photographs in a custom MATLAB program and employed a bilinear scheme to interpolate the deformation between the *unloaded in situ configuration*, i.e., the original 8×8 mm square, and the *unloaded in vitro configuration*. Based on this linear deformation field, $\boldsymbol{\varphi}^r$, we computed the residual deformation gradient tensor $\boldsymbol{F}^r$ as the material gradient of the *unloaded in situ configuration* with respect to the *unloaded in vitro configuration*, i.e., $\boldsymbol{F}^r = \nabla_{\boldsymbol{X}} \boldsymbol{\varphi}^r$. We quantified the residual strain in terms of the Green-Lagrange strain tensor, $\boldsymbol{E}^r = [\boldsymbol{F}^{rT}\boldsymbol{F}^r - \boldsymbol{I}]/2$, where $\mathbf{I}$ is the second order identity tensor. In other words, if skin expanded after incision, these strains would be negative, if skin contracted, they would be positive.

2.5. Planar biaxial testing

Prior to mounting the samples for biaxial testing, we carefully removed the subcutaneous layer and any remaining panniculus carnosus, and speckled the epidermal side with graphite powder. Additionally, before beginning the test protocol, we preloaded the tissue samples equibiaxially to 50 mN to establish a consistent reference state and to remove any tissue slack. Note, we chose 50 mN as the smallest force that we could reliably measure with our load cells. Upon application of the preload, we imaged the original ink pattern one more time to obtain the *preloaded in vitro configuration*. Based on the same process as described in Section 2.4, we also computed a preload deformation gradient tensor, $\boldsymbol{F}^p = \nabla_{\boldsymbol{X}} \boldsymbol{\varphi}^p$, where $\boldsymbol{\varphi}^p$ is the deformation due to preloading. In the actual test protocol, we loaded all samples to 10:20% off-biaxial strain in five cycles of which we recorded the down stroke of the last cycle. We repeated the same protocol for 20:10% off-biaxial strain, and 15:15% equibiaxial strain at a strain rate of approximately 1.25%/s. During testing, we approximated true strains via clamp-to-clamp distance. Simultaneous to the biaxial tests, we continuously captured images of the speckle pattern for off-line digital image correlation at 15 Hz. We performed all tests at 37 °C in 1x PBS and within five hours of excision. After testing, we froze the samples in optimal cutting temperature medium. Subsequently, we sliced two transverse sections of the samples from the center of the tissue and utilized a light microscope to determine tissue thicknesses at several locations, which we later averaged for stress calculations, see Section 2.6.

2.6. Constitutive model fitting

We acquired actual tissue strain during biaxial testing via digital image correlation of the recorded graphite pattern. To this end, we chose the end of the fifth down stroke as the reference configuration to yield the elastic deformation map and deformation gradient, i.e., $\boldsymbol{F}^e = \nabla_{\boldsymbol{X}} \boldsymbol{\varphi}^e$. Note, we disregarded the data of the preconditioning steps as we were interested in the equilibrated tissue response primarily. In the following analysis, we report model fits for stress-stretch data relative to three different reference configurations: (i) relative to the *preloaded in vitro configuration*, i.e., $\boldsymbol{F} = \boldsymbol{F}^e$, (ii) relative to the *unloaded in vitro configuration*, i.e., $\boldsymbol{F} = \boldsymbol{F}^e\boldsymbol{F}^p$, and (iii) relative to the *unloaded in situ configuration*, i.e., $\boldsymbol{F} = \boldsymbol{F}^e\boldsymbol{F}^p\boldsymbol{F}^{-r}$. Moreover, we transformed load data into Cauchy stress via measurements of the sample's thickness and width, which we projected into the current configuration under the assumption of tissue incompressibility.

We fit stress-stretch data from 37 samples to a Fung-type hyperelastic constitutive model superpositioned with a neo-Hookean, isotropic component. Specifically, we employed an invariant-based formulation introduced by Gasser et al. [34],

$$W(\boldsymbol{C}, \boldsymbol{M}) = \mu[I_1 - 3]/2 + k_1[\exp(k_2[\kappa I_1 + [1 - 3\kappa]I_4 - 1]^2) - 1]/[4k_2], \quad (1)$$

where I_1 and I_4 are the first and fourth invariants of the right Cauchy-Green deformation tensor $\boldsymbol{C} = \boldsymbol{F}^T\boldsymbol{F}$, i.e., $I_1 = \boldsymbol{C} : \boldsymbol{I}$ and $I_4 = \boldsymbol{C} : \boldsymbol{M}$, respectively. Here $\boldsymbol{I}$, again, is the second order identity tensor and $\boldsymbol{M}$ is a structural tensor. We computed the structural tensor as $\boldsymbol{M} = \boldsymbol{M}_0 \otimes \boldsymbol{M}_0$, with $\boldsymbol{M}_0 = [\cos(\alpha), \sin(\alpha), 0]$ being the mean fiber orientation vector and α being the mean fiber orientation angle. μ is the shear modulus determining the isotropic material response, while k_1 and k_2 are material parameters determining the anisotropic material response. Both responses are coupled via the fiber dispersion parameter κ, with $\kappa \in [0, 1/3]$, where $\kappa = 0$ enforces a purely anistropic response of the exponential term in Eq. (1), while $\kappa = 1/3$ enforces a purely istropic response of that same term. Note, because we determined tissue thickness after testing, we could not ensure that all samples were tested to a required value of 0.03 MPa. Those data sets that didn't meet the minimum stress requirement were not included in the parameter fit.

Using MATLAB, we performed a nonlinear least-squares fit between the experimentally determined stress-stretch data and the stress-stretch data derived from Eq. (1). Thus, we identified the five unknown material parameters $\mu, k_1, k_2, \alpha, \kappa$ for each sample relative to reference configurations i-iii). See Supplementary Fig. S2 for a representative constitutive fit.

2.7. Statistical analysis

For all data, we used a linear mixed model (LMM) as implemented in R via the package *afex* and performed a Tukey post-hoc analysis, also in R. Statistical significance was defined as p values smaller than 0.05. Data are reported as mean with the standard error of the mean, unless indicated otherwise.

3. Results

Fig. 1A depicts representative histological images of dorsal and ventral murine skin from young (12 weeks) and aged (52 weeks) animals. Masson's Trichrome stain demonstrated the cellular and structural layout of murine skin (left to right) showing: the epidermis, bi-layered dermis, hypodermis, and panniculus carnosus (skeletal muscle). Supplementary Fig. S3 further depicts Picrosirius Red stains of representative samples and illustrates the highly collagenous structure of the murine dermis. Based on the LMM, we found that dermal thickness decreased with age ($p < 0.05$) and that age induced a direction effect ($p < 0.05$), with the post-hoc analysis revealing a significant difference in dermal thickness between young and aged ventral skin ($p < 0.001$) and the dermis being thinner on the ventral side in older mice ($p < 0.05$). Additionally, the hypodermis was thicker in aged mice compared to young mice ($p < 0.05$), again, with age inducing a direction effect ($p < 0.05$). As above, the post-hoc analysis revealed a significant difference on the ventral side between young and aged mice ($p < 0.001$) as well as age inducing regional variation in the hypodermis with it being thicker ventrally in aged mice ($p < 0.05$). We observed no differences in epidermal layer thickness or the muscle/cytoplasm layer thickness, see Fig. 1B. Lastly, analyzing area fractions we did not observe regional or age dependent differences in collagen density (Fig. 1C) [30].

Fig. 2A illustrates sampling regions for 2-photon analysis from the dorsal and ventral locations. For the dorsal samples, we differentiated between cranial and caudal samples, but assumed symmetry across the midline, thus not differentiating between the left and right lateral samples. Fig. 2B illustrates representative *in vitro*

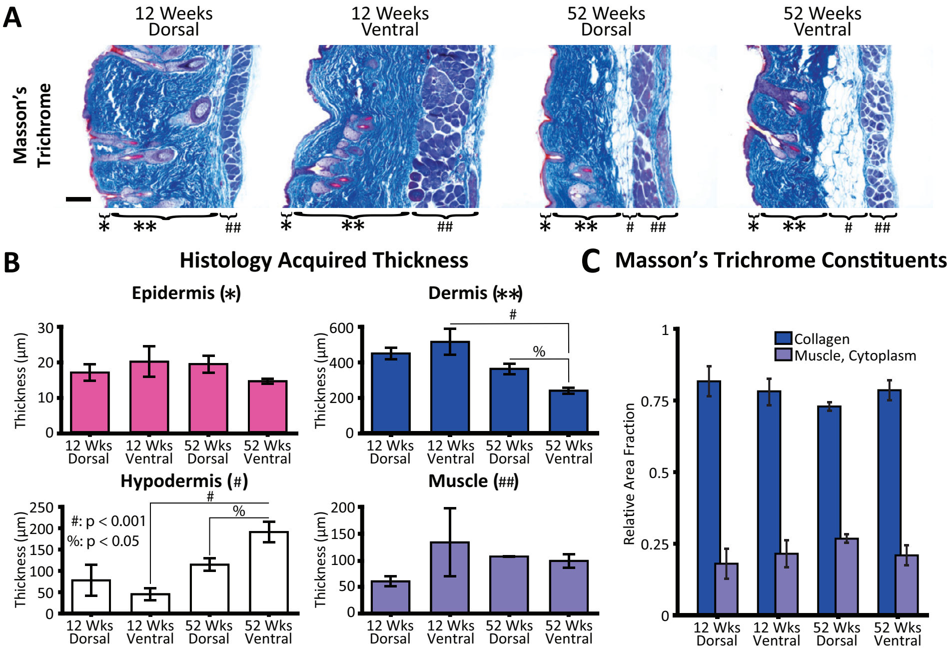

Fig. 1. Histological analysis of dorsal and ventral skin samples from young (12 weeks) and aged (52 weeks) mice reveal differences in layer thickness with age. Using Masson's Trichrome, collagen stains blue, and cytoplasm and muscle stain red. A) Representative cross-sectional images revealing murine skin's layered structure with (left to right) the epidermal layer (*), the dermal layer (**), hypodermis (including adipose tissue) (#) and skeletal muscle layer (##). B) Estimates of relative mass density based on area fractions of collagen and cytoplasm/muscle for 12 samples. C) Layer thickness analysis of 12 histological slides. For all analyses, n=3 for each young/aged, dorsal/ventral group. (Scale bar = 100 µm). (For interpretation of the references to color in this figure legend, the reader is referred to the web version of this article.)

2-photon images taken in the dermal layer as well as a depth-dependent analysis of the collagen fiber orientation probability distribution function, which were averaged among all samples. Qualitatively, these data suggest that collagen fibers are widely dispersed with a mean orientation in lateral direction (i.e., orthogonally to the cranial-caudal axis) and without significant variation in depth (at least to the measured depth of ~100–150µm) (Fig. 2B). Similarly, Fig. 2C illustrates the same data collected in the post-mortem, *in situ* configuration, i.e., without excising the tissue, but from different animals. Here again, qualitative observation suggests that collagen fibers *in situ* have a mean distribution in the lateral direction, are widely dispersed, and do not significantly vary with depth. Statistically comparing the location parameter of the von Mises distribution for sample location, age, z-stack depth, and *in situ versus in vitro* configuration revealed a difference only in location ($p < 0.001$). Specifically, we found that cranial dorsal samples have a mean direction larger than 90°, i.e., they are oriented slightly in caudal direction, as opposed to all other regions. Statistical comparison between the concentration parameter revealed, again, a difference in location ($p < 0.01$), but also a difference with depth ($p < 0.001$). Specifically, the concentration parameter decreases with depth, i.e., fiber orientations become more dispersed.

Table 1 summarizes the location parameter $\tilde{\mu}$ and concentration parameter $\tilde{\kappa}$ for the *in vitro* and *in situ* configurations as a function of location, age, region, and depth. Note, the von Mises distribution parameters $\tilde{\mu}$ and $\tilde{\kappa}$ should not be confused with the constitutive parameters of our Fung-type material law, μ and κ. Moreover, please note that the concentration parameter is inversely related to the variance. Therefore, a decrease in the concentration parameter indicates an increase in variance.

Our methodology for the residual/prestrain analysis is summarized in Fig. 3A. We found that skin samples shrunk upon excision as quantified by Green-Lagrange strain. Strain appeared highly region-dependent ($p < 0.001$). Specifically, we found that ventral samples shrunk 11.4 ± 2.6% in the lateral direction and 9.0 ± 2.3% in cranial-caudal direction in young mice and in the same directions by 14.5 ± 3.0% and 13.7 ± 2.8% in aged mice (Fig. 3B). Only small differences as a function of direction or age were observed, regardless of location, neither of which reached statistical significance. Shear strains were negligibly small and less than 2% for all groups. Fig. 3C illustrates strain induced via preloading to 50 mN. We found that small preloads of 50 mN imposed impressively large deformations on the skin samples before the beginning of the biaxial tests. In fact, Green-Lagrange strains due to preloading varied between ~20% and ~90% depending on location ($p < 0.005$), age ($p = 0.52$), and direction ($p < 0.005$).

Fig. 4A shows a representative skin sample in (i) the *preloaded in vitro configuration*, (ii) the *loaded in vitro configuration* under equibiaxial stretch, and (iii) the sample's mechanical response. In Fig. 4B, we report skin stiffness as the tangent moduli (i.e., the slopes to the equibiaxial data) in the "toe-region" of the stress-stretch curves and in "calf-region" at 0.03 MPa. Additionally, we quantify curve shifts on the stretch axis by determining the stretch at which the stress reached 0.03 MPa. We chose 0.03 MPa as the stress that most samples reached during testing, excluding those from analysis which would require data extrapolation. We found that the toe-region stiffness significantly varied between the lateral and cranial-caudal direction ($p < 0.05$), with skin being stiffer in lateral direction, but found no difference with age or region. In contrast, we did not find any differences in the calf-region stiffness with direction, age, or location. Finally, the stretch at 0.03 MPa was significantly different in direction ($p < 0.001$) and location ($p < 0.001$), but not with age. Together, these results show that murine skin stiffens at a smaller stretch in lateral direction relative to the midline direction and on the dorsal side relative to the ventral side. Note, while we did not demonstrate a main effect of age in the in the stretch at 0.03 MPa ($p = 0.094$), we did identify an age-induced increase on the ventral side in the cranial-caudal direction ($p < 0.005$), which we included in Fig. 4B.

Fig. 5 illustrates the predicted equibiaxial constitutive behavior of murine skin based on the assumption of three different

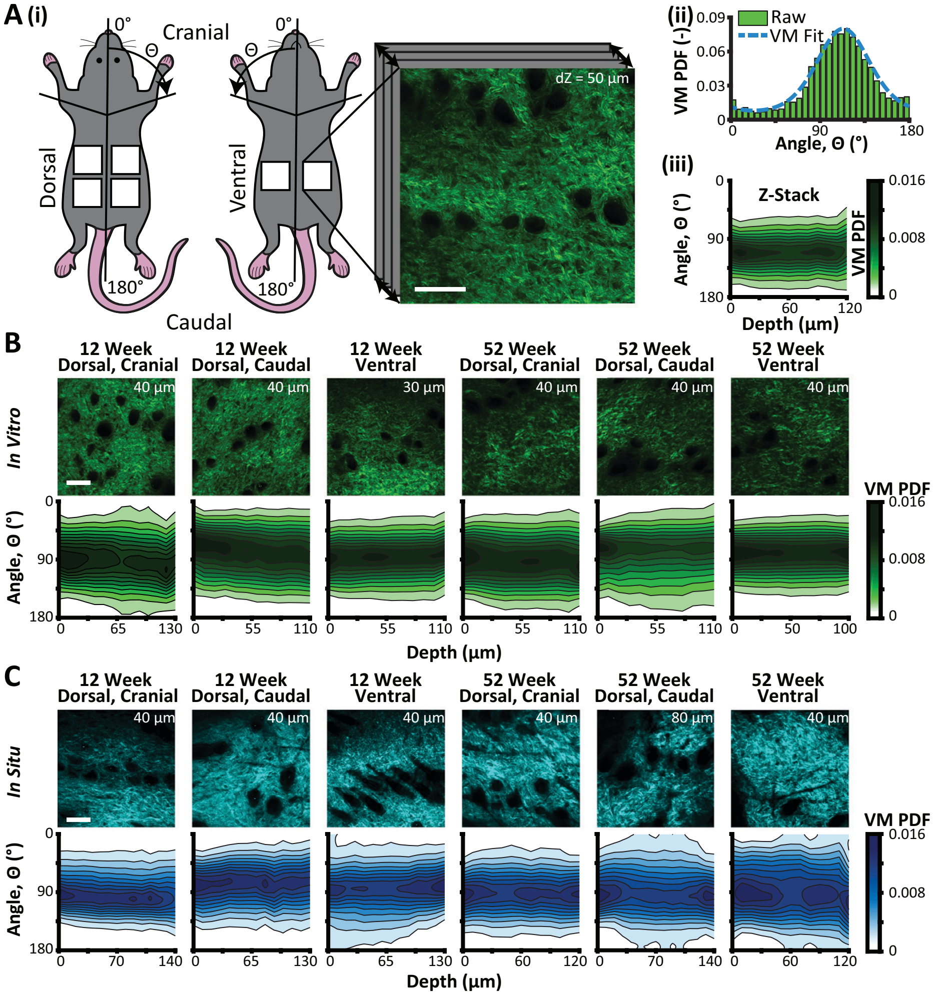

Fig. 2. 2-photon analysis of skin samples from young (12 weeks) and aged (52 weeks) mice reveal that collagen is widely distributed with the mean direction pointing laterally. A) We excited second harmonic generation signals at 900 nm, which we epi-collected with a 460 ± 25 nm PMT filter at 0–150 μm depth. Using a plugin to NIH's ImageJ, OrientationJ, we derived orientation histograms for each depth and fit a symmetric von Mises distribution to these data. Representative B) *in vitro* and C) *in situ* images with average von Mises distributions throughout thickness for young and aged mice, for each location. Note, circular black regions in the 2-photon images are hair follicles. For *in situ* and *in vitro* analyses, $n = 3$ for each young/aged, dorsal/ventral group. (Scale bar = 100 μm).

reference configurations, as per Eq. (1) (see Method Section 2.6). Informed via off-biaxial and equibiaxial data, Fig. 5A depicts the response of dorsal and ventral skin of young and aged mice assuming that the preloaded reference configuration is stress-free, i.e., $\boldsymbol{F} = \boldsymbol{F}^e$ (average root-mean-square error: 0.01 MPa). The curves show the classic J-shaped trajectory of soft collagenous tissues. All curves cluster, thus giving the impression of, at most, marginal regionally- and age-dependent differences in the material response of murine skin. Moreover, differences in the (i) lateral direction and (ii) cranial-caudal direction, appear trivial. Instead, defining the *in situ* configuration as the reference configuration, i.e., $\boldsymbol{F} = \boldsymbol{F}^e\boldsymbol{F}^p\boldsymbol{F}^{-r}$, Fig. 5B demonstrates the biaxial constitutive behavior of dorsal and ventral skin of young and aged mice ignoring residual strain (average root-mean-square error: 0.01 MPa). Albeit qualitatively similar, the curves shift significantly toward larger stretches in comparison to the curves in Fig. 5A. Furthermore, the curves begin to spread along the stretch axis. Specifically, these curves demonstrate a larger shift in the stretch direction of the 52-week-old skin, for both dorsal and ventral samples. That is, aged skin appears to be more compliant than young skin when deformation is calculated relative to the unloaded *in situ* configuration. Finally, Fig. 5C depicts the constitutive behavior of murine skin, provided a truly stress-free reference configuration, i.e., with respect to the unloaded *in vitro* configuration $\boldsymbol{F} = \boldsymbol{F}^e\boldsymbol{F}^p$ (average root-mean-square error: 0.01 MPa). Naturally, in this scenario curves are shifted the farthest to the right on the stretch-axis. Additionally, the spread between curves increases further showing distinct behaviors of murine skin in young and aged mice, where the aged skin has shifted even farther to the right on the stretch axis suggesting that aged skin is more compliant than young skin. The mean material parameters for the Holzapfel material model of Eq. (1) are listed in Table 2 as a function of region and age.

4. Discussion

Mice are the most widely used animal model for human related disease research and are the model of choice for skin research. The ability of skin to resist deformation is a critical component of its functionality and increasing effort has been invested in characterizing the mechanical behavior of murine skin. However, our collective knowledge of mouse skin biomechanics shows some critical gaps related to how murine skin behaves under directional stress. Here we simultaneously investigated age-, regional-, and direction-dependent characteristics of mouse skin mechanics and demonstrate the biaxial mechanical behavior of murine skin. Finally, we quantified residual strain in mouse skin, which is critical to

Table 1
Mean and concentration of von Mises distributions representing the collagen fiber orientations derived from 2-photon microscopy dependent on age, location, imaging depth, and *in vitro vs. in situ* imaging.

Depth(μm)	12 Wks, Dorsal, Cranial		12 Wks, Dorsal, Caudal		12 Wks, Ventral		52 Wks, Dorsal, Cranial		52 Wks, Dorsal, Caudal		52 Wks Ventral	
	$\tilde{\mu}(^\circ)$	$\tilde{\kappa}(-)$	$\tilde{\mu}(^\circ)$	$\tilde{\kappa}(-)$	$\tilde{\mu}(^\circ)$	$\tilde{\kappa}(-)$	$\tilde{\mu}(^\circ)$	$\tilde{\kappa}(-)$	$\tilde{\mu}(^\circ)$	$\tilde{\kappa}(-)$	$\tilde{\mu}(^\circ)$	$\tilde{\kappa}(-)$
In Vitro												
0	86.3 ± 6.7	1.37 ± 0.23	74.8 ± 15.1	1.11 ± 0.38	88.8 ± 6.0	2.04 ± 0.25	88.1 ± 9.6	1.94 ± 0.31	87.3 ± 18.8	2.35 ± 1.04	83.2 ± 6.7	2.47 ± 0.36
10	88.2 ± 9.4	1.68 ± 0.13	79.9 ± 20.1	1.37 ± 0.33	88.3 ± 6.9	1.78 ± 0.12	87.4 ± 10.5	1.75 ± 0.21	84.3 ± 16.1	1.87 ± 0.65	83.5 ± 6.5	2.07 ± 0.22
20	88.6 ± 9.3	1.56 ± 0.09	80.8 ± 19.6	1.26 ± 0.28	89.0 ± 7.2	1.78 ± 0.13	89.7 ± 10.3	1.51 ± 0.21	86.6 ± 19.0	1.58 ± 0.47	83.4 ± 6.3	1.89 ± 0.20
30	88.8 ± 9.4	1.40 ± 0.08	79.4 ± 18.2	1.26 ± 0.17	88.2 ± 7.0	1.69 ± 0.13	92.0 ± 10.7	1.44 ± 0.18	86.8 ± 20.1	1.41 ± 0.54	83.1 ± 6.4	1.81 ± 0.18
40	89.9 ± 9.9	1.33 ± 0.09	80.7 ± 20.3	1.21 ± 0.12	88.5 ± 6.3	1.68 ± 0.13	93.8 ± 10.3	1.32 ± 0.15	86.2 ± 18.4	1.37 ± 0.50	82.9 ± 5.8	1.77 ± 0.20
50	90.4 ± 9.8	1.35 ± 0.08	82.4 ± 18.4	1.16 ± 0.12	89.0 ± 6.5	1.62 ± 0.16	93.3 ± 9.8	1.33 ± 0.11	88.6 ± 20.1	1.32 ± 0.50	83.2 ± 6.3	1.68 ± 0.20
60	90.7 ± 9.8	1.22 ± 0.08	82.6 ± 20.2	1.10 ± 0.10	88.2 ± 6.9	1.55 ± 0.16	93.4 ± 9.5	1.30 ± 0.08	87.2 ± 20.0	1.27 ± 0.50	82.7 ± 6.0	1.66 ± 0.17
70	92.0 ± 10.0	1.09 ± 0.12	83.7 ± 19.5	1.11 ± 0.02	87.8 ± 7.1	1.55 ± 0.16	93.2 ± 10.0	1.36 ± 0.09	87.1 ± 19.7	1.23 ± 0.47	82.1 ± 6.1	1.64 ± 0.17
80	91.3 ± 7.6	1.04 ± 0.16	84.8 ± 20.0	1.11 ± 0.02	87.6 ± 6.8	1.51 ± 0.18	91.9 ± 10.2	1.29 ± 0.09	87.8 ± 20.3	1.25 ± 0.51	81.6 ± 5.6	1.62 ± 0.17
90	93.1 ± 7.1	1.09 ± 0.17	83.5 ± 19.3	1.07 ± 0.05	86.6 ± 6.4	1.50 ± 0.18	91.0 ± 10.2	1.29 ± 0.10	84.5 ± 16.1	1.22 ± 0.47	82.2 ± 5.3	1.69 ± 0.26
100	93.5 ± 7.5	1.03 ± 0.16	84.3 ± 19.4	1.09 ± 0.06	87.6 ± 6.1	1.54 ± 0.22	91.8 ± 10.2	1.21 ± 0.12	83.4 ± 16.4	1.23 ± 0.48	81.0 ± 3.4	1.66 ± 0.23
In Situ												
0	85.0 ± 5.7	1.99 ± 0.46	82.1 ± 4.7	1.46 ± 0.23	85.4 ± 9.5	1.71 ± 0.27	97.3 ± 3.6	1.33 ± 0.27	86.7 ± 6.9	1.69 ± 0.32	81.1 ± 9.7	1.12 ± 0.13
10	85.6 ± 6.2	1.85 ± 0.41	86.0 ± 6.8	1.47 ± 0.18	99.4 ± 9.6	1.63 ± 0.30	92.8 ± 5.0	1.21 ± 0.22	84.1 ± 6.2	1.52 ± 0.37	81.9 ± 8.3	1.15 ± 0.12
20	87.3 ± 5.4	1.70 ± 0.42	84.4 ± 6.3	1.38 ± 0.20	83.9 ± 10.1	1.48 ± 0.23	92.4 ± 6.1	1.09 ± 0.18	82.6 ± 6.4	1.34 ± 0.27	83.2 ± 8.6	1.13 ± 0.12
30	88.4 ± 6.1	1.68 ± 0.41	81.8 ± 5.8	1.29 ± 0.16	84.9 ± 9.1	1.48 ± 0.29	93.5 ± 5.7	1.03 ± 0.20	83.9 ± 7.0	1.09 ± 0.16	85.3 ± 8.6	1.11 ± 0.13
40	89.8 ± 6.2	1.66 ± 0.35	79.4 ± 5.9	1.30 ± 0.21	84.9 ± 9.1	1.49 ± 0.30	94.1 ± 4.5	1.02 ± 0.21	85.4 ± 7.6	1.01 ± 0.15	86.5 ± 8.7	1.08 ± 0.11
50	90.3 ± 6.7	1.71 ± 0.40	79.2 ± 6.1	1.23 ± 0.15	85.0 ± 9.1	1.39 ± 0.20	92.0 ± 6.4	1.03 ± 0.23	84.3 ± 7.9	0.98 ± 0.15	86.2 ± 9.0	0.99 ± 0.11
60	90.4 ± 6.3	1.62 ± 0.39	79.4 ± 6.1	1.22 ± 0.16	84.7 ± 8.7	1.40 ± 0.18	90.9 ± 7.2	1.11 ± 0.21	86.2 ± 7.9	0.98 ± 0.14	85.1 ± 9.0	0.86 ± 0.11
70	90.4 ± 6.5	1.56 ± 0.38	80.9 ± 7.1	1.18 ± 0.17	86.2 ± 8.4	1.33 ± 0.19	93.9 ± 4.5	1.11 ± 0.21	87.8 ± 8.2	1.05 ± 0.13	83.8 ± 8.7	0.85 ± 0.11
80	90.4 ± 6.3	1.69 ± 0.49	79.0 ± 5.6	1.31 ± 0.17	86.2 ± 7.7	1.41 ± 0.20	92.8 ± 5.1	1.06 ± 0.22	86.2 ± 8.6	0.97 ± 0.15	87.3 ± 9.0	0.93 ± 0.10
90	92.0 ± 6.0	1.78 ± 0.55	84.4 ± 7.1	1.24 ± 0.15	86.0 ± 7.6	1.39 ± 0.19	92.7 ± 5.4	1.08 ± 0.22	87.2 ± 8.3	1.05 ± 0.20	87.8 ± 8.7	0.86 ± 0.12
100	91.5 ± 7.2	1.63 ± 0.44	83.3 ± 8.8	1.16 ± 0.19	80.2 ± 6.4	1.37 ± 0.16	94.5 ± 5.2	1.05 ± 0.22	86.0 ± 7.5	0.98 ± 0.20	86.5 ± 8.8	0.74 ± 0.12

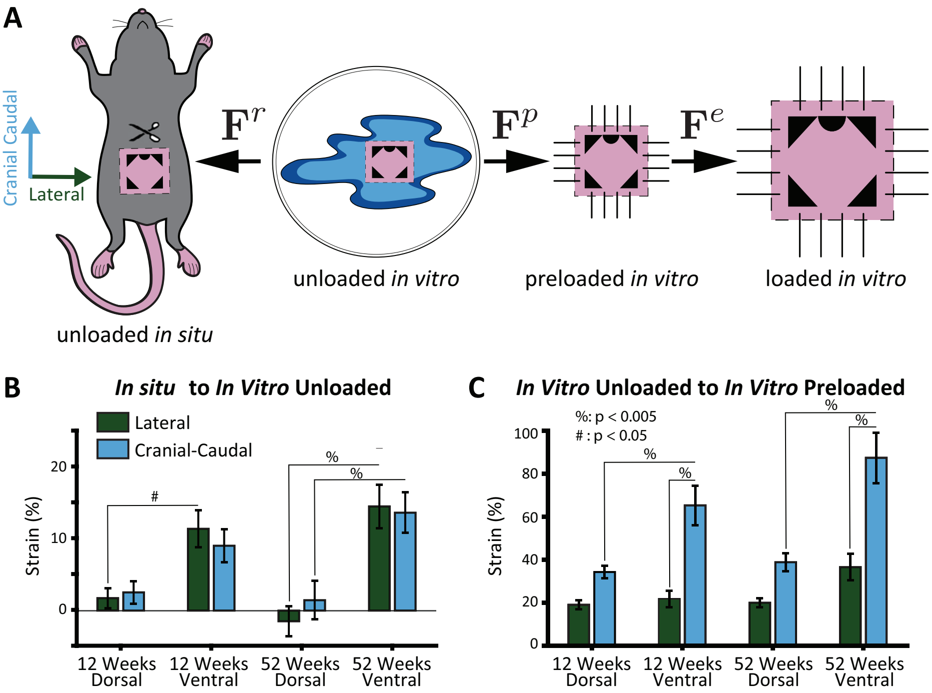

Fig. 3. Residual strain and pre-strain analysis of dorsal and ventral skin samples from young (12 weeks) and aged (52 weeks) mice reveal that ventral mouse skin is under residual strain *in situ*. (A) We stamped skin regions *in situ* ("unloaded *in situ* configuration") before excising them and photographing them floating on 1x PBS ("unloaded *in vitro* configuration") and after applying 50 mN of equibiaxial preload ("preloaded *in vitro* configuration"). Note, samples were photographed within minutes from excisions. Using a large deformation kinematic approach, we computed the respective deformation gradients to compute Green-Lagrange strain between each configuration. (B) Green-Lagrange strain between the unloaded *in vitro* configuration and unloaded *in situ* configuration, i.e., residual strain. (C) Green-Lagrange strain between the unloaded *in vitro* configuration and preloaded *in vitro* configuration, i.e., prestrain. For residual strain and pre-strain analysis, $n = 13$ for each young/aged, dorsal/ventral group.

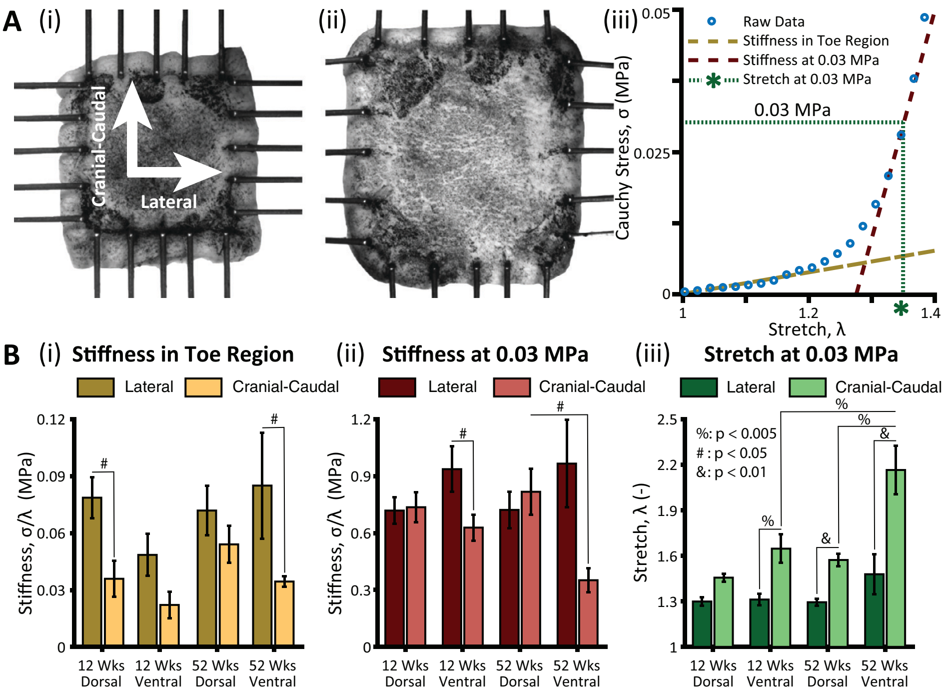

Fig. 4. Biaxial skin mechanics show differences in tangent modulus with direction (at 0.03 MPa) and demonstrate that mouse skin becomes more compliant with age on the ventral side. (A) A representative skin sample in the (i) unloaded *in vitro* configuration, the (ii) equibiaxially loaded *in vitro* configuration, and (iii) the mechanical response of a representative skin sample in the lateral direction to equibiaxial loading. (B) (i)Toe-region stiffness, (ii) calf-region stiffness, and (iii) stretch at 0.03 MPa as they vary with direction, region, and age. For these analyses, only samples which reached 0.03 MPa were included: Young Dorsal $n = 10$, Young Ventral $n = 7$, Aged Dorsal $n = 7$, Aged Ventral $n = 4$.

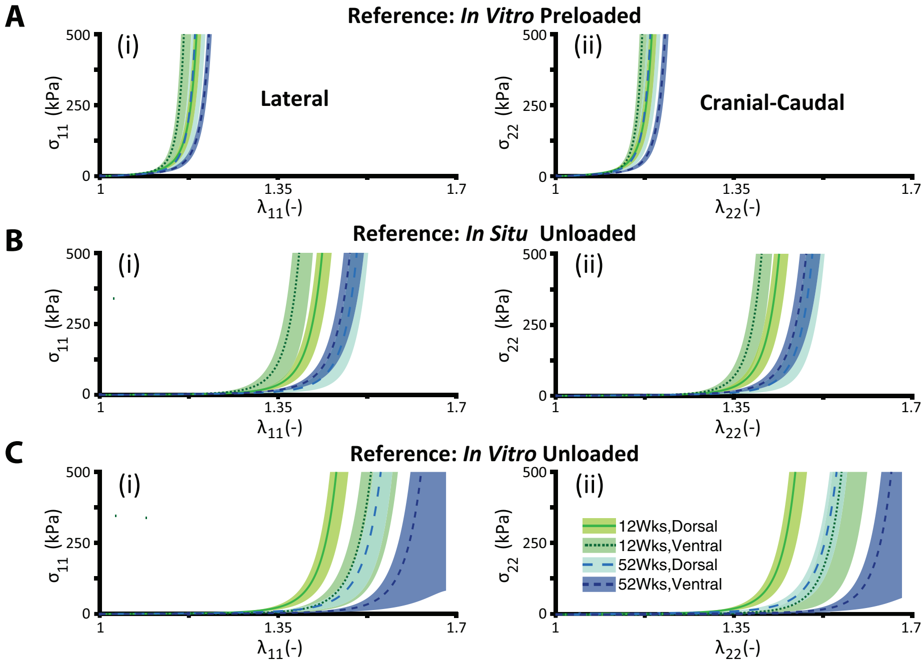

Fig. 5. Constitutive response (mean ± standard error) of dorsal and ventral skin samples from young (12 weeks) and aged (52 weeks) mice significantly varies depending on the choice of reference configurations. (A) Response to equibiaxial loading based on the preloaded *in vitro* reference configuration in (i) lateral direction and (ii) cranial-caudal direction. (B) Response to equibiaxial loading based on the unloaded *in situ* reference configuration in (i) lateral direction and (ii) cranial-caudal direction. (C) Response to equibiaxial loading based on the unloaded *in vitro* reference configuration in (i) lateral direction and (ii) cranial-caudal direction. For these analyses: Young Dorsal $n = 11$, Young Ventral $n = 7$, Aged Dorsal $n = 9$, Aged Ventral $n = 10$. Note, while only the constitutive response to equibiaxial data is shown, these fits where informed by all biaxial protocols, including off-biaxial protocols.

Table 2
Mean material parameters for the Holzapfel material model [34] for young and aged mice, for both regions, and all three reference configurations. These parameters were determined via simultaneous fits to the down-strokes of the fifth equi- and off-biaxial loading cycles. For these analyses: Young Dorsal $n = 11$, Young Ventral $n = 7$, Aged Dorsal $n = 9$, Aged Ventral $n = 10$.

Preloaded *In Vitro* Configuration						
	μ (MPa)	$k1$(MPa)	$k2$ (-)	α (°)	κ(-)	RMSE (MPa)
Young Dorsal	3.89e-03 ± 4.70e-03	4.87e-01 ± 5.54e-01	94.01 ± 76.00	82.13 ± 49.54	0.26 ± 0.08	0.012 ± 0.008
Young Ventral	2.92e-03 ± 3.63e-03	2.02e-01 ± 1.28e-01	100.80 ± 87.12	82.01 ± 35.45	0.23 ± 0.08	0.011 ± 0.011
Aged Dorsal	5.93e-03 ± 5.93e-03	3.51e-01 ± 4.11e-01	110.84 ± 89.29	110.00 ± 70.66	0.28 ± 0.06	0.009 ± 0.010
Aged Ventral	6.19e-03 ± 4.57e-03	1.73e-01 ± 1.57e-01	96.59 ± 63.12	98.12 ± 50.86	0.27 ± 0.04	0.006 ± 0.004
Unloaded *In Vivo* Configuration						
Young Dorsal	8.57e-04 ± 1.24e-03	2.03e-02 ± 1.59e-02	13.27 ± 6.03	76.20 ± 52.85	0.29 ± 0.05	0.012 ± 0.007
Young Ventral	5.43e-04 ± 7.93e-04	1.88e-02 ± 1.85e-02	15.32 ± 7.26	102.86 ± 31.49	0.28 ± 0.03	0.010 ± 0.010
Aged Dorsal	2.06e-03 ± 1.93e-03	1.17e-02 ± 2.21e-02	8.71 ± 5.18	74.47 ± 41.69	0.27 ± 0.10	0.010 ± 0.010
Aged Ventral	1.13e-03 ± 1.87e-03	2.25e-02 ± 1.67e-02	8.31 ± 5.19	80.32 ± 43.30	0.30 ± 0.04	0.007 ± 0.004
Unloaded *In Vitro* Configuration						
Young Dorsal	6.82e-04 ± 1.01e-03	1.78e-02 ± 1.64e-02	11.13 ± 4.12	81.82 ± 25.87	0.29 ± 0.06	0.013 ± 0.008
Young Ventral	4.04e-04 ± 4.46e-04	2.39e-03 ± 3.09e-03	3.74 ± 1.55	94.60 ± 11.26	0.18 ± 0.08	0.010 ± 0.010
Aged Dorsal	1.64e-03 ± 1.68e-03	1.49e-02 ± 1.12e-02	5.94 ± 3.90	110.00 ± 66.33	0.31 ± 0.02	0.011 ± 0.010
Aged Ventral	3.19e-04 ± 3.21e-04	7.79e-03 ± 1.24e-02	2.08 ± 1.68	99.01 ± 42.50	0.27 ± 0.06	0.007 ± 0.004

accurate models of mouse skin mechanics, and may be an important mechanical marker of skin health.

4.1. The effect of age

Comparing animals in early (12 weeks) and late adulthood (52 weeks) we found that the composition, microstructural organization, and general mechanics of murine skin were, at most, marginally changed during normal aging. We found that as mice age, the dermis becomes thinner and the hypodermis increases its adipose fraction on the ventral side. A deeper analysis using 2-photon microscopy showed marginal changes in the microstructural organization of collagen. Although the mean fiber direction significantly shifted in some regions, those changes were minimal and are unlikely of mechanical significance. While our limited analysis of collagen content revealed no changes in collagen density between young and aged mice, total collagen content (as the product of dermal thickness and collagen area fraction) decreased with age. With respect to stiffness, there appears to be no agreed upon definition of stiffness to describe the mechanical behavior of mouse skin. While stiffness in general denotes some relationship between stress and strain, there is no *one* stiffness value that can sufficiently describe a non-linear material such as skin. Hence, a tangent modulus, i.e., a stiffness for a given strain or stretch, may be the best option for reducing an analysis to one single metric. The only other publication on the mechanical properties of aging murine skin reports stiffness values as the tangent modulus to the “linear portion” of a uniaxial stress-strain curve [9]. However, this study did not report the stretch at which this modulus was computed. Moreover, their reference configuration was defined as the stretch at which no further vertical displacement of their sample was observed under the 2-photon microscope, which is difficult to reproduce. Finally, Lynch et al. did not precondition their skin samples. Lack of these data makes a quantitative comparison with our data difficult. However, it appears that our data qualitatively agree with their findings and they also report an age-induced increase in the stretch at which they observed the tissue’s “toe-region”, i.e., with age the stress-stretch curves shifted toward larger stretch suggesting that skin becomes more compliant. In contrast to Lynch et al., however, we found that our tangent modulus at 0.03 MPa didn’t increase with age. Differences may be due to any of above limitations of their study. Overall, marginal changes between young and aged mice are likely due to our “old” mice only being 52 weeks old as opposed to, say 60–80 weeks, as in Lynch et al.’s study. Future studies will extend our analysis to mice of older age.

4.2. Heterogeneity

All previous studies of mouse skin have focused on either dorsal skin samples [9,17,35,36], or ventral skin samples [18], but not both. The only exceptions are studies by Karimi et al., who omitted any discussion on variations in skin behavior between the two regions [22], and Seifert et al., whose analysis focused on work to fracture [37]. In this study, we found that murine skin properties do vary by anatomic locations. Although skin composition did not vary between the dorsal and ventral side in young mice, age induced a marked difference between the two locations in dermal thickness and adipose deposition. While we found that concentration of collagen orientation varied between the dorsal and the ventral side, as do the mean fiber directions, those changes were small and are unlikely to affect the mechanical behavior of the skin. In addition to age-related alterations in skin layer thickness, we also found that residual strain varied by location such that ventral skin is subject to significant residual strain, while dorsal skin is not. Finally, we found the mechanical response of murine skin had an earlier stiffening point (i.e., toe-region) in the dorsal *versus* ventral region. Although, it is unclear what causes these mechanical differences between the dorsal and the ventral skin samples, it may be hypothesized that they are functionally related to differences in dynamic range during daily use (i.e., ventral skin may undergo larger deformations and may thus have adapted accordingly). Note, in addition to heterogeneity between skin regions, there may also be heterogeneity within samples. In our current work, we collect samples of small dimensions (8 × 8 mm) to minimize within-sample variation. However, future studies may combine spatially-resolved strain maps with inverse analyses to correlate variations in tissue composition and structure with changes in mechanical properties. Such findings may reveal the structure-function relationship of skin at a sub-millimeter scale.

4.3. Anisotropy

Skin is famously anisotropic with Langer having meticulously mapped out the axes of skin anisotropy across the whole human body [38]. Mouse skin, just like human skin, was previously shown to be mechanically anisotropic [8]. It is understood that the direction of highest stiffness in soft collagenous tissues is determined by the mean fiber direction of the tissue's extracellular matrix [39]. Our data support this understanding with 2-photon-derived collagen orientation probability functions showing means that coincide with directions of higher toe-region and calf-region stiffness. We would like to note, however, that collagen fibers in our study were broadly distributed with large variances, a finding that renders the idea of perfectly "aligned" fibers an oversimplification.

4.4. Residual strain & reference configuration

Residual strain is a known phenomenon in many engineering materials, but most characteristic for living materials [40–42]. Fung et al. famously performed opening angle experiments on segments of the aorta [43]. Since then, residual strains have been demonstrated in many other tissues. They are characterized by their presence despite the absence of external forces. Human skin is known for its demonstration of residual strain [44,45]. However, residual strains have never been demonstrated in murine skin. Indication of residual strain may be an indicator of tissue health and thus it is important to understand if it occurs in particular tissues. Specifically, residual strains likely arise from deposition of collagen at a prestretch by fibroblasts and thus this measure may be a surrogate for a healthy matrix turnover which in turn indicates an equilibrated mechanobiological balance of resident skin cells [25,26]. Additionally, residual strains markedly alter the mechanical behavior of soft tissues, largely owing to the multiplicative nature of the deformation gradient under large deformation. Thus, even small amounts of residual strain can, when omitted, result in drastically erroneous predictions. For example, we found residual strains, predominantly in ventral skin samples, on the order of $\sim$10% which can result in errors of the same magnitude if omitted. Interestingly, we did not observe any gross microstructural differences between the dorsal and ventral side that would explain the absence and presence of residual strain in the respective samples. Future studies that include analyses of fiber crimp and fiber-matrix coupling may be able to explain our observations.

4.5. Constitutive model

This is the first study to have biaxially informed a material law for mouse skin. Although others have studied mouse skin in various directions using repeated uniaxial tensile tests, those tests do not excite the biaxial coupling modes of skin and can thus not replace actual biaxial tests. To this end, we chose a Fung-type, invariant-based, hyperelastic material law suggested and popularized by Gasser et al. [34]. Among the advantages of this law are (i) its applicability to large deformations and compatibility with the finite element framework, (ii) its microstructural motivation and thus the possibility of interpreting its material constants in a non-phenomenological manner, (iii) its implementation in most commercial and non-commercial finite element packages, and (iv) its consistently good fits to the J-shaped material behavior observed in all collagenous soft tissues.

Interestingly, the material parameters identified for the Holzapfel model indeed reflect the microstructural information as observed via 2-photon analysis. Specifically, α and κ, the mean fiber angle and the fiber dispersion parameter of the Holzapfel model, reflect the location parameter and concentration parameter of the von Mises distributions describing the collagen orientation as measured via 2-photon microscopy. While at first this may not appear surprising, it implies i) an inherent consistency between the microstructural data and the force data that informed the constitutive fit, and ii) that the constitutive model as suggested by Holzapfel et al. indeed allows for a microstructural interpretation of its parameters. The latter point dictates a superiority of this model over other, more phenomenological ones.

In our current work, we chose to model skin samples as a homogenous membrane. In fact, skin is a multi-layered structured as revealed in our histological data. Therefore, future studies may attempt to separate skin layers and test their histomechanics individually toward layered models of murine mouse skin.

We are reporting the mean material parameters for all groups and for all reference configurations. Thus, when using our material parameters to model murine skin, the modeler can choose to impose our reported residual strains in the *unloaded in situ configuration* and subsequently use the material parameters as reported for the *unloaded in vitro configuration*. Alternatively, the modeler can choose to model mouse skin as stress-free in the *unloaded in situ configuration* and use our material parameters as determined using the *unloaded in situ configuration* as the reference.

4.6. Relationship between murine and human skin

Mice are the most common model for human skin disease. For example, mouse models have been used to study basic wound healing biology, hypertrophic scarring, and chronic wounds [46–49]. The use of murine skin models is motivated by a common skin structure. Skin in both species consists of a superficial epithelial layer (epidermis), a connective tissue layer beneath it (dermis), and a subcutaneous fatty layer (hypodermis). However, there are also significant differences between murine skin and human skin [49]. Murine skin has a subcutaneous layer of skeletal muscle called the panniculus carnosus which is not present in humans with few focal exceptions. The panniculus carnosus is apparent as mouse skin is loose, i.e., unattached from underlying tissues, unlike in humans. This anatomical difference impacts the wound healing response. Murine wounds heal primarily by contraction, whereas human skin healing is driven by granulation tissue remodeling and re-epithelialization. Additionally, mice do not have rete ridges at the interface between epidermis and dermis whereas humans do. Mouse skin is also thinner and more compliant with respect to human skin. Also, mouse skin has a high hair density with a 3-week hair cycle, whereas human skin hair density is highly variable between individual and depends on anatomical location. Differences in follicle density should be considered before extrapolating information on skin from mice to human. Finally, we found that Movat's Pentachrome staining (data not shown) revealed little to no elastin staining in either young or aged skin samples. As elastin effects the elastic recoil of skin, it may be critical to investigate in the future to what degree elastin content differs between murine and human skin and how a possible discrepancy may affect mouse skin as a mechanical model for human skin [50].

Anatomic similarities between human and murine skin lead to similarities in mechanical properties [8]. Mechanical testing of human skin has revealed characteristic features of collagenous soft tissues, demonstrating anisotropy and nonlinear behavior that can be captured with microstructurally-based strain energy functions [6,51–54]. We and others have shown that murine skin behaves similarly. While it is possible that anatomical and structural differences between murine and human skin can lead to specific differences in mechanics, this remains to be studied in detail. For instance, the hair cycle has been shown to alter hypodermis thickness, but its effect on mechanical properties has not been resolved [20].

In humans, age induces thinning of the dermis and increases skin laxity as compared to young adults [55,56]. Both results are congruent with our results of aged murine skin. In humans, age also induces changes in tissue stiffness, notwithstanding the concept of stiffness is rather vague for a nonlinear material. For instance, a vast collection of suction test data suggests that older adults have stiffer skin [57], which aligns with previous work on murine skin [9]. However, in the current study, we don't find the same trend, although we do observe a shift of the stress-strain behavior of murine skin toward larger strains. Therefore, reports of stiffening or softening of skin with aging must be further studied, both for murine and human skin, under the premise of using more detailed, nonlinearly sensitive metrics for “stiffness”.

4.7. Limitations

We see the largest limitation of our study in the use of 52 week-old mice as representative for old age. As pointed out in Section 4.1, Lynch et al. used 60–80 week-old mice and reported significantly stiffer behavior of the skin in terms of the tangent modulus. Thus, the reader may be warned that our data is representative for post-reproductive, late-adulthood rather than old age, which is why we refer to the older group as “aged” throughout the manuscript. Moreover, we computed collagen content as a function of region and age using histology-based area fractions. Of course, this approach is limited to a two-dimensional analysis and thus is insensitive to three-dimensional variations. Therefore, our inability to demonstrate differences in collagen content with region and age, may, at least in part, also be related to this limitation. Additionally, our 2-photon analysis is limited to a depth of ∼100 µm, at which point our SHG signal diminished. In the future, we plan on performing optical clearing to increase the penetration depth. However, given the clear trend toward depth-independence of the SHG signal, we doubt that there would be drastic changes at deeper tissue levels. Also, by reporting tissue stress as force divided by current area, we implicitly assumed that skin is homogeneous throughout its thickness. Given the layered structure of skin this is only an approximation. However, given that the dermis occupies most of the tissue’s cross-section, this homogenization is a good approximation of the stress state for most of the tissue. Lastly, we used a depilatory agent to remove hair from the mouse skin. While we minimize exposure time and use an FDA-approved agent, there is a potential risk that it may alter skin properties slightly.

4.8. Conclusions

In this current work, we present a comprehensive study on murine skin mechanics. Combining histology, 2-photon microscopy, and detailed biaxial mechanical tests, we delineate regional-, age-, and directionally-dependent structural, microstructural, and stress-strain responses of mouse skin. Moreover, we cast the mechanical behavior of mouse skin into a versatile constitutive law. In detail, we re-confirm that mouse skin shows the classic J-shaped constitutive behavior of all collagenous soft tissues, that it is anisotropic with the predominant direction being lateral, which is explained by the microstructural organization of its extracellular matrix, and that it shows significant variations between the ventral and dorsal side. Additionally, we found that skin is under significant residual strain, albeit, mostly on the ventral side. Importantly, we find that inclusion of residual strains in the mechanical analysis of mouse skin significantly alters the stress-strain curves and should always be considered in models. Lastly, we found that the skin of mice at 52 weeks, representative for late adulthood, shows only marginal differences to the skin of young mice. Structurally, aged skin becomes thinner and fattier. Mechanically, aged skin’s stress-strain curve shifts toward larger strains, i.e., becomes more compliant, but the tangent modulus at a stretch representative of calf-region of the stress-strain curve does not change significantly. In conclusion, our study fills significant gaps in our knowledge of mouse skin. Besides adding to our basic biomechanical understanding of mouse skin, our data will be valuable as baseline data for future studies on genetically modified animals or other strains and provides critical data toward accurate models of mouse skin.

Declaration of Competing Interest

None of the authors have any conflicts to declare.

Acknowledgment

This research was partially conducted with support from the National Science Foundation to Adrian B. Tepole and Manuel K. Rausch (Grant # 1916663).

Supplementary materials

Supplementary material associated with this article can be found, in the online version, at doi:10.1016/j.actbio.2019.10.020.

References

[1] A.B. Tepole, M. Gart, A.K. Gosain, E. Kuhl, Characterization of living skin using multi-view stereo and isogeometric analysis, Acta Biomater. 10 (2014) 4822–4831, doi:10.1016/j.actbio.2014.06.037.

[2] V.R. Sherman, Y. Tang, S. Zhao, W. Yang, M.A. Meyers, Structural characterization and viscoelastic constitutive modeling of skin, Acta Biomater. 53 (2017) 460–469, doi:10.1016/j.actbio.2017.02.011.

[3] M.L. Crichton, B.C. Donose, X. Chen, A.P. Raphael, H. Huang, M.A.F. Kendall, The viscoelastic, hyperelastic and scale dependent behaviour of freshly excised individual skin layers, Biomaterials 32 (2011) 4670–4681, doi:10.1016/j.biomaterials.2011.03.012.

[4] R. Oftadeh, B.K. Connizzo, H.T. Nia, C. Ortiz, A.J. Grodzinsky, Biological connective tissues exhibit viscoelastic and poroelastic behavior at different frequency regimes: Application to tendon and skin biophysics, Acta Biomater. 70 (2018) 249–259, doi:10.1016/j.actbio.2018.01.041.

[5] Y. Wang, K.L. Marshall, Y. Baba, E.A. Lumpkin, G.J. Gerling, Compressive viscoelasticity of freshly excised mouse skin is dependent on specimen thickness, strain level and rate, PLoS One (2015) 10, doi:10.1371/journal.pone.0120897.

[6] T.K. Tonge, L.S. Atlan, L.M. Voo, T.D. Nguyen, Full-field bulge test for planar anisotropic tissues: Part I-Experimental methods applied to human skin tissue, Acta Biomater. 9 (2013) 5913–5925, doi:10.1016/j.actbio.2012.11.035.

[7] T.K. Tonge, L.M. Voo, T.D. Nguyen, Full-field bulge test for planar anisotropic tissues: Part ii-a thin shell method for determining material parameters and comparison of two distributed fiber modeling approaches, Acta Biomater. 9 (2013) 5926–5942, doi:10.1016/j.actbio.2012.11.034.

[8] R.B. Groves, S.A. Coulman, J.C. Birchall, S.L. Evans, An anisotropic, hyperelastic model for skin: Experimental measurements, finite element modelling and identification of parameters for human and murine skin, J. Mech. Behav. Biomed. Mater. 18 (2013) 167–180, doi:10.1016/j.jmbbm.2012.10.021.

[9] B. Lynch, C. Bonod-Bidaud, G. Ducourthial, J.S. Affagard, S. Bancelin, S. Psilodimitrakopoulos, F. Ruggiero, J.M. Allain, M.C. Schanne-Klein, How aging impacts skin biomechanics: a multiscale study in mice, Sci. Rep. 7 (2017) 13750, doi:10.1038/s41598-017-13150-4.

[10] H. Adhoute, J. de Rigal, J.P. Marchand, Y. Privat, J.L. Leveque, Influence of age and sun exposure on the biophysical properties of the human skin: an *in vivo* study, Photodermatol. Photoimmunol. Photomed. 9 (1992) 99–103 http://www.ncbi.nlm.nih.gov/pubmed/1300143. (accessed February 4, 2019).

[11] G.E. Piérard, C. Letawe, A. Dowlati, C. Piérard-Franchimont, Effect of hormone replacement therapy for menopause on the mechanical properties of skin, J. Am. Geriatr. Soc. 43 (1995) 662–665, doi:10.1111/j.1532-5415.1995.tb07202.x.

[12] B. Hansen, G.B.E. Jemec, The mechanical properties of skin in osteogenesis imperfecta, Arch. Dermatol. 138 (2002) 909–911, doi:10.1001/archderm.138.7.909.

[13] D.T. Corr, D.A. Hart, Biomechanics of scar tissue and uninjured skin, Adv. Wound Care 2 (2013) 37–43, doi:10.1089/wound.2011.0321.

[14] M.J. Arin, D.R. Roop, Inducible mouse models for inherited skin diseases: Implications for skin gene therapy, Cells Tissues Organs 177 (2004) 160–168, doi:10.1159/000079990.

[15] P. Avci, M. Sadasivam, A. Gupta, W.C. De Melo, Y.-Y. Huang, R. Yin, R. Chandran, R. Kumar, A. Otufowora, T. Nyame, M.R. Hamblin, Animal models of skin disease for drug discovery, Expert Opin. Drug Discov. 8 (2013) 331–355, doi:10.1517/17460441.2013.761202.

[16] M. Bouclier, D. Cavey, N. Kail, C. Hensby, Experimental models in skin pharmacology, Anim. Models Used Cuatneous Pharmacol. (1990) 127–154, doi:10.1007/978-1-4684-7902-7_6.

[17] S. Bancelin, B. Lynch, C. Bonod-Bidaud, G. Ducourthial, S. Psilodimitrakopoulos, P. Dokládal, J.M. Allain, M.C. Schanne-Klein, F. Ruggiero, Ex vivo multiscale quantitation of skin biomechanics in wild-type and genetically-modified mice using multiphoton microscopy, Sci. Rep. 5 (2015) 17635, doi:10.1038/srep17635.

[18] M.J. Muñoz, J.A. Bea, J.F. Rodríguez, I. Ochoa, J. Grasa, A. Pérez del Palomar, P. Zaragoza, R. Osta, M. Doblaré, An experimental study of the mouse skin behaviour: damage and inelastic aspects, J. Biomech. 41 (2008) 93–99, doi:10.1016/j.jbiomech.2007.07.013.

[19] S.C. Meliga, J.W. Coffey, M.L. Crichton, C. Flaim, M. Veidt, M.A.F. Kendall, The hyperelastic and failure behaviors of skin in relation to the dynamic application of microscopic penetrators in a murine model, Acta Biomater. 48 (2017) 341–356, doi:10.1016/j.actbio.2016.10.021.

[20] Y. Wang, K.L. Marshall, Y. Baba, G.J. Gerling, E.A. Lumpkin, Hyperelastic material properties of mouse skin under compression, PLoS One 8 (2013) 67439, doi:10.1371/journal.pone.0067439.

[21] A. Karimi, R. Faturechi, M. Navidbakhsh, S.A. Hashemi, Nonlinear hyperelastic behavior to identify the mechanical properties of rat skin under uniaxial loading, J. Mech. Med. Biol. 14 (2014) 1450075, doi:10.1142/S0219519414500754.

[22] A. Karimi, S.M. Rahmati, M. Navidbakhsh, Mechanical characterization of the rat and mice skin tissues using histostructural and uniaxial data, Bioengineered 6 (2015) 153–160, doi:10.1080/21655979.2015.1036202.

[23] M.S. Sacks, Biaxial mechanical evaluation of planar biological materials, J. Elast. 61 (2000) 199–246, doi:10.1023/A:1010917028671.

[24] G.A. Holzapfel, R.W. Ogden, On planar biaxial tests for anisotropic nonlinearly elastic solids. a continuum mechanical framework, Math. Mech. Solids 14 (2009) 474–489, doi:10.1177/1081286507084411.

[25] J.D. Humphrey, E.R. Dufresne, M.A. Schwartz, Mechanotransduction and extracellular matrix homeostasis, Nat. Rev. Mol. Cell Biol. 15 (2014) 802–812, doi:10.1038/nrm3896.

[26] J.D. Humphrey, K.R. Rajagopal, A constrained mixture model for growth and remodeling of soft tissues, Math. Model. Methods Appl. Sci. 12 (2002) 407–430, doi:10.1142/S0218202502001714.

[27] A. Buganza Tepole, M. Gart, C.A. Purnell, A.K. Gosain, E. Kuhl, The incompatibility of living systems: characterizing growth-induced incompatibilities in expanded skin, Ann. Biomed. Eng. 44 (2016) 1734–1752, doi:10.1007/s10439-015-1467-4.

[28] M.K. Rausch, N. Famaey, T.O.B. Shultz, W. Bothe, D.C.C. Miller, E. Kuhl, Mechanics of the mitral valve: a critical review, an *in vivo* parameter identification, and the effect of prestrain, Biomech. Model. Mechanobiol. 12 (2013) 1053–1071, doi:10.1007/s10237-012-0462-z.

[29] M.K. Rausch, E. Kuhl, On the effect of prestrain and residual stress in thin biological membranes, J. Mech. Phys. Solids 61 (2013) 1955–1969, doi:10.1016/j.jmps.2013.04.005.

[30] J.D. Humphrey, M.R. Bersi, R. Khosravi, A.J. Wujciak, D.G. Harrison, Differential cell-matrix mechanoadaptations and inflammation drive regional propensities to aortic fibrosis, aneurysm or dissection in hypertension, J. R. Soc. Interface (n.d.). doi:10.1098/rsif.2017.0327.

[31] M.D. Abràmoff, P.J. Magalhães, S.J. Ram, Image processing with ImageJ, Biophotonics Int. 11 (2004) 36–41, doi:10.1117/1.3589100.

[32] R. Rezakhaniha, A. Agianniotis, J.T.C. Schrauwen, A. Griffa, D. Sage, C.V.C. Bouten, F.N. Van De Vosse, M. Unser, N. Stergiopulos, J.T.C. Schrauwen, A. Griffa, D. Sage, C.V.C. Bouten, A. Agianniotis, Experimental investigation of collagen waviness and orientation in the arterial adventitia using confocal laser scanning microscopy, Biomech. Model. Mechanobiol. 11 (2012) 461–473, doi:10.1007/s10237-011-0325-z.

[33] A.J. Schriefl, A.J. Reinisch, S. Sankaran, D.M. Pierce, G.A. Holzapfel, Quantitative assessment of collagen fibre orientations from two-dimensional images of soft biological tissues, J. R. Soc. Interface (n.d.). doi:10.1098/rsif.2012.0339.

[34] T.C. Gasser, R.W. Ogden, G.A. Holzapfel, Hyperelastic modelling of arterial layers with distributed collagen fibre orientations, J. R. Soc. Interface 3 (2006) 15–35, doi:10.1098/rsif.2005.0073.

[35] B. Lynch, S. Bancelin, C. Bonod-Bidaud, J.B. Gueusquin, F. Ruggiero, M.C. Schanne-Klein, J.M. Allain, A novel microstructural interpretation for the biomechanics of mouse skin derived from multiscale characterization, Acta Biomater. 50 (2017) 302–311, doi:10.1016/j.actbio.2016.12.051.

[36] S. Nesbitt, W. Scott, J. Macione, S. Kotha, Collagen fibrils in skin orient in the direction of applied uniaxial load in proportion to stress while exhibiting differential strains around hair follicles, Mater. (Basel) 8 (2015) 1841–1857, doi:10.3390/ma8041841.

[37] A.W. Seifert, S.G. Kiama, M.G. Seifert, J.R. Goheen, T.M. Palmer, M. Maden, Skin shedding and tissue regeneration in African spiny mice (Acomys), Nature 489 (2012) 561–565, doi:10.1038/nature11499.

[38] K. Langer, On the anatomy and physiology of the skin, Br. J. Plast. Surg. 31 (1978) 3–8, doi:10.1016/0007-1226(78)90003-6.

[39] M.S. Sacks, D.B. Smith, E.D. Hiester, A small angle light scattering device for planar connective tissue microstructural analysis, Ann. Biomed. Eng. 25 (1997) 678–689, doi:10.1007/BF02684845.

[40] E. Lejeune, C. Linder, Modeling mechanical inhomogeneities in small populations of proliferating monolayers and spheroids, Biomech. Model. Mechanobiol. 17 (2018) 727–743, doi:10.1007/s10237-017-0989-0.

[41] P.J. Withers, H.K.D.H. Bhadeshia, Residual stress. Part 2 – nature and origins, Mater. Sci. Technol. 17 (2001) 366–375, doi:10.1179/026708301101510087.

[42] M. Genet, M.K. Rausch, L.C. Lee, S. Choy, X. Zhao, G.S. Kassab, S. Kozerke, J.M. Guccione, E. Kuhl, Heterogeneous growth-induced Prestrain in the heart, J. Biomech. 48 (2015) 2080–2089, doi:10.1016/j.jbiomech.2015.03.012.

[43] S.Q. Liu, Y.C. Fung, Zero-Stress states of arteries, 1988. https://biomechanical.asmedigitalcollection.asme.org (accessed January 24, 2019).

[44] D. Pond, A.T. Mcbride, L.M. Davids, B.D. Reddy, G. Limbert, Microstructurally-based constitutive modelling of the skin - Linking intrinsic ageing to microstructural parameters, J. Theor. Biol. 4 (2018) 108–123, doi:10.1016/j.jtbi.2018.01.014.

[45] J. Weickenmeier, M. Jabareen, E. Mazza, Suction based mechanical characterization of superficial facial soft tissues, J. Biomech. 48 (2015) 4279–4286, doi:10.1016/J.JBIOMECH.2015.10.039.

[46] T.V. Boyko, M.T. Longaker, G.P. Yang, Laboratory models for the study of normal and pathologic wound healing, Plast. Reconstr. Surg. 139 (2017) 654–662, doi:10.1097/PRS.0000000000003077.

[47] J.M. Davidson, Animal models for wound repair, Arch. Dermatol. Res. 290 (1998) 1–11.

[48] R.D. Galiano, J. Michaels V, M. Dobryansky, J.P. Levine, G.C. Gurtner, Quantitative and reproducible murine model of excisional wound healing, Wound Repair Regen. 12 (2004) 485–492, doi:10.1111/j.1067-1927.2004.12404.x.

[49] G.C. Gurtner, V.W. Wong, M. Sorkin, J.P. Glotzbach, M.T. Longaker, Surgical approaches to create murine models of human wound healing, J. Biomed. Biotechnol. 2011 (2011), doi:10.1155/2011/969618.

[50] H. Oxlund, J. Manschot, A. Viidik, The role of elastin in the mechanical properties of skin, J. Biomech. 21 (1988) 213–218, doi:10.1016/0021-9290(88)90172-8.

[51] C. Flynn, A.J. Taberner, P.M.F. Nielsen, S. Fels, Simulating the three-dimensional deformation of *in vivo* facial skin, J. Mech. Behav. Biomed. Mater. 28 (2013) 484–494, doi:10.1016/j.jmbbm.2013.03.004.

[52] N. Kumaraswamy, H. Khatam, G.P. Reece, M.C. Fingeret, M.K. Markey, K. Ravi-Chandar, Mechanical response of human female breast skin under uniaxial stretching, J. Mech. Behav. Biomed. Mater. 74 (2017) 164–175, doi:10.1016/j.jmbbm.2017.05.027.

[53] A. Wahlsten, M. Pensalfini, A. Stracuzzi, G. Restivo, R. Hopf, E. Mazza, On the compressibility and poroelasticity of human and murine skin, Biomech. Model. Mechanobiol. 18 (2019) 1079–1093, doi:10.1007/s10237-019-01129-1.

[54] A. Ní Annaidh, K. Bruyère, M. Destrade, M.D. Gilchrist, M. Otténio, Characterization of the anisotropic mechanical properties of excised human skin, J. Mech. Behav. Biomed. Mater. 5 (2012) 139–148, doi:10.1016/j.jmbbm.2011.08.016.

[55] C.H. Daly, G.F. Odland, Age-related changes in the mechanical properties of human skin, J. Invest. Dermatol. 73 (1979) 84–87, doi:10.1111/1523-1747.ep12532770.

[56] A.B. Cua, K.P. Wilhelm, H.I. Maibach, Elastic properties of human skin: relation to age, sex, and anatomical region, Arch. Dermatol. Res. 282 (1990) 283–288, doi:10.1007/BF00375720.

[57] S. Luebberding, N. Krueger, M. Kerscher, Mechanical properties of human skin in vivo: A comparative evaluation in 300 men and women, Ski. Res. Technol. 20 (2014) 127–135, doi:10.1111/srt.12094.